World Scientific
www.worldscientific.com

Accurate Multi-Physics Numerical Analysis of Particle Preconcentration Based on Ion Concentration Polarization

Zirui Li*, Wei Liu and Lingyan Gong

*Institute of Laser and Optoelectronic Intelligent
Manufacturing, College of Mechanical and Electrical Engineering
Wenzhou University, Wenzhou, P. R. China*

*lizirui@gmail.com

Yudan Zhu

*State Key Laboratory of Materials-Oriented Chemical Engineering
College of Chemical Engineering, Nanjing Tech University
Nanjing, P. R. China*

Yuantong Gu

*School of Chemistry, Physics and Mechanical Engineering
Queensland University of Technology, Australia*

Jongyoon Han

*Department of Electrical Engineering and Computer Science
Department of Biological Engineering
Massachusetts Institute of Technology Cambridge
Massachusetts, USA*

*Singapore-MIT Alliance for Research
and Technology, Singapore*

This paper studies the mechanism of preconcentration of charged particles in a straight microchannel embedded with permselective membranes by numerically solving the coupled transport equations of ions, charged particles and solvent fluid without any simplifying assumptions. It is demonstrated that trapping and preconcentration of charged particles are determined by the interplay between drag force from the electroosmotic fluid flow and the electrophoretic force applied through the electric field. Several insightful characteristics are revealed, including the diverse dynamics of co-ions and counter ions, replacement of co-ions by focused particles, lowered ion concentrations in particle-enriched zone, and enhanced electroosmotic pumping effect, etc. Conditions for particles that can be concentrated are identified in terms of charges, sizes and electrophoretic mobilities of particles and co-ions. Dependences of enrichment factor on cross-membrane voltage, initial particle concentration and buffer ion concentrations are analyzed and the underlying reasons are elaborated. Finally, *post priori* condition for the validity of decoupled simulation model is given based on the charges carried by focused particles

and buffer co-ions. These results provide an important guidance in the design and optimization of nanofluidic preconcentration and other related devices.

Keywords: Electrokinetic preconcentration; ion concentration polarization; electroosmotic flow.

1. Introduction

Electrokinetic manipulation for electrolytes and particles in micro and nanoscale fluidic systems experienced significant progresses in the last decade [Çetin *et al.*, 2014]. While electroosmotic flow (EOF) has been well characterized in microfluidics [Auroux *et al.*, 2002], transport behaviors of ion and fluids in nanoscale channels or pores are much less understood [Sparreboom *et al.*, 2010]. Overlapping electric double layers (EDLs) generate a lot of new physics and invoked many novel applications. Basically, inside nanoscale spaces, the amount of counter ions is significantly greater than that of co-ions [Bocquet and Charlaix, 2010]. When a nanochannel is used to bridge two microchannels and an electric field is applied along the channel axis (as shown in Fig. 1(a)), the number of counter ions transported is significantly greater than that of co-ions, rendering ion current permselective. This selective charge transport results in ion depletion and enrichment zones in either side of the nanochannel, also known as ion concentration polarization (ICP). Such micro/nanofluidic systems facilitate many unique and novel functionalities, such as desalination [Nikonenko *et al.*, 2014; Kim *et al.*, 2010a; Deng *et al.*, 2015], particle preconcentration [Wang *et al.*, 2005; Kim *et al.*, 2010b; Lin *et al.*, 2011] and biomolecular separation, etc. [Li and Anand, 2016; Napoli *et al.*, 2010]. Because materials containing nanoscale pores with charged surfaces have the same ion exclusion effects, permselective membranes (e.g., Nafion) are widely used to substitute nanochannels, eliminating the need for more involved nanoscale fabrications.

Physics underlying the nanofluidic ICP is complicated [Zangle *et al.*, 2010a]. It involves coupled nonlinear fluid flow, ionic transport, dynamic evolution of electric potential and sometimes deformation of polymeric channel structures [Li *et al.*, 2016; Drozdov and Christiansen, 2016]. In addition to ICP, selective transport of ions across the nanochannels induces a strong electric field and an extended space charge layer at the depletion side, which produces a fast, vortical, sometimes even chaotic fluid flow under the external electric field [Kim *et al.*, 2009]. Study of such complicated systems has been largely based on experimental observation of tracing particles. Unfortunately, however, direct experimental monitoring of some key parameters (e.g., ion concentrations) in such micro/nanofluidic systems is still impractical, prohibiting the accurate understanding of the system. Precise description of mechanisms has to rely on numerical simulation. In this aspect, there have been some simulation studies on ICP propagation [Mani *et al.*, 2009; Zangle *et al.*, 2009, 2010b], vortical flow [Dydek *et al.*, 2011; Druzgalski *et al.*, 2013; Rubinstein and Zaltzman, 2015; Yossifon *et al.*, 2009; Liu *et al.*, 2018] and desalination
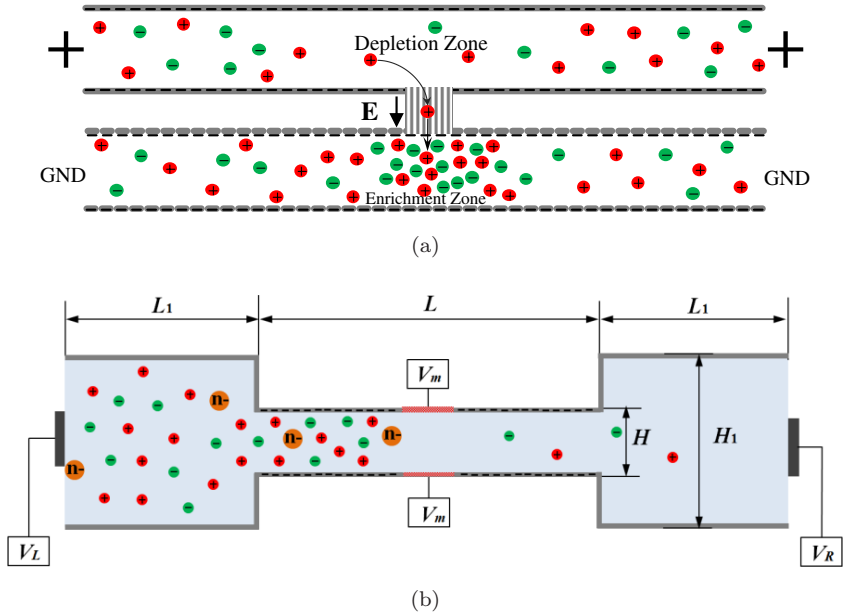
(a)

(b)

Fig. 1. (a) Schematic sketch of ICP systems. (b) Physical setup of particle preconcentration system.

of solution of binary ions [Hlushkou *et al.*, 2016]. However, very few simulation studies have been reported for preconcentration processes. Recently, Shen *et al.* [2010] simulated EOF-driven protein preconcentration process in a microchannel integrated with Nafion strip. They used constant zeta potential to describe the surface charge effect and did not consider the effect of (accumulated) charged proteins on the distribution of electric field. These assumptions will become invalid when high variation of electric field is involved and/or high level of charged protein concentration is achieved, as often encountered in preconcentration experiments for low abundance proteins. Wang *et al.* [2009] conducted a more accurate simulation for pressure-driven particle preconcentration and established the dependence of the focusing rate upon diffusivity and electrophoretic mobility of particles. Yet, their simple model does not involve coupled fluid flow and is limited to extremely slow flow conditions.

The purpose of this paper is to study the mechanism of charged particle preconcentration through accurate multi-physics modeling without any simplifying assumptions. Mechanisms underlying the particle enrichment will be elaborated in terms of interplay between the viscous drag force and the electrophoretic force applied on the charged particles. Condition for particle enrichment will be identified. By analyzing eventual steady states of the system, replacement of co-ions by the focused particles and its consequences will be elaborated. Finally, a dynamic picture for transport of ions, particles and fluids is given to offer a new way of explaining experimental data and guiding the design of relevant systems.

2. Methods

2.1. *System setup*

Figure 1(b) shows a schematic of two-dimensional model for particle preconcentration simulation. The key component of the system is a microchannel of length $L = 120\,\mu\text{m}$ and width $H = 4\,\mu\text{m}$ embedded with permselective membranes of length $L_m = 2\,\mu\text{m}$ in the middle of both top and bottom walls. Connected to the microchannel are two wider channel segments of length $L_1 = 60\,\mu\text{m}$ and width $H_1 = 120\,\mu\text{m}$ (simulating part of the reservoirs). The microchannel walls are charged with density $\sigma_- = -5\,\text{mC/m}^2$, while walls of wider channels are uncharged. The left boundary is connected to a mixed solution of potassium chloride (KCl) and negatively charged particles (denoted by P^{n-}, with n representing the valence number). An electric field is applied such that the voltage at the left boundary is $V_L = 20V_T$ ($V_T = 25.8\,\text{mV}$ is the thermal voltage) and that at the right boundary is $V_R = 0$, inducing an EOF from left to right. Pressures at both the left and the right boundaries are set to zero such that transport of ions and fluids is resulting from electrokinetic phenomena only. The permselective membranes are assumed to permit passage of cations only. Concentration of cations required to neutralize the fixed charge density inside the membrane is C_m. Voltages at the membrane surface are independently set to V_m. For convenience, a term cross-membrane voltage $V_{cm} = (V_L + V_R)/2 - V_m$ is defined as the difference between voltage at the membrane location determined by external electric field without ICP and the actual voltage applied on the membrane, representing the voltage drop across the microchannel/membrane junction in actual experiments. Lower V_m corresponds to larger V_{cm} and generates stronger ion depletion effect.

2.2. *Governing equations*

Governing equations for the incompressible fluid flow, ionic and particle transport, and electric potential are described by the Navier–Stokes (NS), Nernst–Planck and Poisson equations, respectively [Rubinstein and Zaltzman, 2000; Pham *et al.*, 2012]:

$$\rho(\partial \mathbf{U}/\partial t + (\mathbf{U} \cdot \nabla)\mathbf{U}) = -\nabla P + \eta \nabla \cdot \nabla \mathbf{U} - \rho_e \nabla \Phi, \tag{1}$$

$$\nabla \cdot \mathbf{U} = 0, \tag{2}$$

$$\frac{\partial C_i}{\partial t} = -\nabla \cdot \mathbf{J}_i, \tag{3}$$

$$\mathbf{J}_i = -(D_i \nabla C_i + Z_i(D_i F/RT)C_i \nabla \Phi) + \mathbf{U}C_i, \tag{4}$$

$$-\nabla \cdot (\varepsilon \nabla \Phi) = \rho_e. \tag{5}$$

Here, $\mathbf{U}$ is the velocity, P is the pressure, C_i and $\mathbf{J}_i$ are the concentration and flux density of species i, respectively. For convenience, we use $i = 1$ for K$^+$, $i = 2$ for Cl$^-$, and $i = 3$ for P^{n-}. Z_i and D_i are the valence and diffusion coefficient of species i, respectively. Φ is the electric potential, $\rho_e = e \sum_{i=1}^{3} Z_i C_i$ is the free space charge

density, with e being the elementary charge. Parameters ρ, η and ε are the mass density, dynamic viscosity and permittivity of the solution, respectively. T is the absolute temperature. Constants F and R are Faraday's number and gas constant, respectively.

2.3. *Boundary conditions*

At the membrane's surfaces, it is assumed that [Rubinstein and Zaltzman, 2000; Pham *et al.*, 2012] (i) Fluxes of anions and particles across the membrane are zero; (ii) The concentration of cations at the membrane surface is C_m; (iii) The electric potential at the membrane surface is V_m; (iv) The membrane surface is impermeable and no-slip to fluid, indicating zero velocity and zero-gradient condition for the pressure. The corresponding equations are

$$\mathbf{J}_2 \cdot \mathbf{n} = 0, \quad \mathbf{J}_3 \cdot \mathbf{n} = 0, \quad C_1 = C_m, \quad \Phi = V_m, \quad \mathbf{U} = \mathbf{0}. \tag{6}$$

Here, $\mathbf{n}$ is the normal vector perpendicular to the boundary pointing out of the fluid domain.

At microchannel walls, the boundary conditions are (i) constant surface charge density σ_-; (ii) no-slip condition for fluid velocity and (iii) impermeability to ions and particles:

$$\nabla \Phi = -\sigma_- / \varepsilon, \quad \mathbf{U} = \mathbf{0}, \quad \mathbf{J}_i \cdot \mathbf{n} = 0, \quad i = 1, 2, 3. \tag{7}$$

At the inlet boundary, (i) both concentrations of electrolytes and particles are the same as those in the inlet reservoir, (ii) the electric potential is V_L and (iii) the pressure is zero:

$$\Phi = V_L, \quad \nabla \mathbf{U} \cdot \mathbf{n} = \mathbf{0}, \quad P = 0, \quad C_i = C_{i,0}, \quad i = 1, 2, 3. \tag{8}$$

At outlet boundary, (i) *free* boundary conditions are applied for fluid flow and (ii) the electric potential is set to V_R:

$$\Phi = V_R, \quad \nabla \mathbf{U} \cdot \mathbf{n} = \mathbf{0}, \quad P = 0, \quad \nabla C_i \cdot \mathbf{n} = 0, \quad i = 1, 2, 3. \tag{9}$$

At reservoir walls, the boundary conditions are (i) no-slip condition for fluid velocity and zero-gradient condition for pressure and (ii) zero charge:

$$\mathbf{U} = \mathbf{0}, \quad \nabla P \cdot \mathbf{n} = 0, \quad \nabla \Phi \cdot \mathbf{n} = 0. \tag{10}$$

2.4. *Numerical methods*

In this work, the governing equations are solved with the specified boundary conditions using COMSOL v5.2a (a full model is provided as supplemental information). Based on symmetries in geometry and physics setup, only the lower half of the channel is modeled with symmetric boundary conditions at the upper boundary of the calculation model (the central line of the channel). The computational domain is meshed using quadrilateral elements. Finer grids are adopted near the charged

walls, membrane surfaces, inlet and outlet boundaries of the channel. Concentration and potential fields are implemented in physics interfaces of Transport of Diluted Species and Electrostatics interface. The Poisson–Nernst–Planck (PNP) equations are solved using quadratic Lagrange interpolation functions for space discretization. NS and continuity equations are implemented in Creeping Flow interface. Quadratic Lagrange shape functions are used for NS equations whereas linear functions are used for the continuity equation.

For time-dependent analysis, we adopt two different configurations at different stages of simulation. At the beginning stage ($t \leq 0.5$ s), PNP and NS equations are solved segregatedly [Karatay *et al.*, 2015]. At each time step, the velocity and pressure are solved first (with electric force calculated from the charges at the previous step), followed by concentrations and potentials (with the velocity and pressure obtained at this step). Default setting of multi-frontal massively parallel sparse direct solver (MUMPS) is adopted with an implicit generalized α method ($\alpha = 0.99$). In this stage, ion-depletion zone emerges and vortices are generated. After that, fully coupled PNP and NS equations are solved using backward differentiation formula (BDF) method with free time steps, until the end of simulation time.

For steady state analysis, fully coupled PNP and NS equations are solved using default solver (automatic Newton nonlinear method). Due to the strong nonlinear characteristics of the system and the inconsistency in the initial conditions for concentration and electric potential near the channel or membrane surfaces, it is necessary to ramp up the membrane voltages slowly to the desired value. This is implemented through auxiliary sweep of parameters within the solver.

3. Results and Discussions

3.1. *Developments of particle concentration and concentration speed*

We start with a time-dependent simulation for the enrichment of divalent particles P^{2-} ($Z_3 = -2$, $n = 2$) of diameter four times larger than Cl^- ($D_3 = D_2/4$, because diffusion coefficient of a spherical particle is inversely proportional to its diameter) at $V_{cm} = 30V_T$. The initial concentrations are the same as those in the reservoir ($C_{1,0} = 1$ mM, $C_{3,0} = 10^{-7}$ mM and $C_{2,0} = C_{1,0} - 2C_{3,0}$). The Debye length $\lambda_D = \sqrt{\varepsilon RT/2C_0F^2}$ is about 9.6 nm, corresponding to a dimensionless Debye length 0.0048 with respect to half of the microchannel width ($2\,\mu$m). This setup guarantees that the system runs in a diluted solution regime, which does not involve correction of fluid properties, such as density and viscosity, even when the particles are focused (actually, the focused particles will replace co-ions and reduce the concentration of buffer ions, making the solution diluter, cf. Sec. 3.5). As the boundary condition, the concentration of K^+ at the membrane surface is $C_m = 2$ mM.

Figure 2(a) shows the evolution of particle concentration inside the microchannel (colors not to scale, concentration values can be found in the corresponding
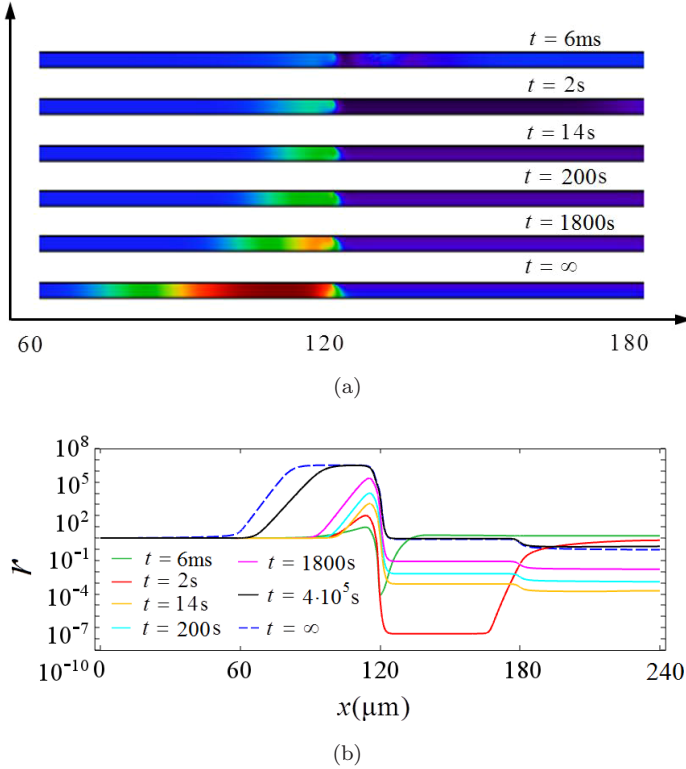
(a)

(b)

Fig. 2.   Concentration of P^{2-} at different times: (a) two-dimensional distributions (colors not to scale) and (b) profiles of enrichment factor r along the center line of the channel.

curves in Fig. 2(b)). It could be found that shortly after application of V_{cm} (e.g., $t = 6$ ms), particles begin to accumulate in the upstream microchannel and the enrichment factor $r = C_3/C_{3,0}$ grows. In the mean time, particle concentration near the membrane location is lowered and this low concentration region expands to the downstream with the fluid flow. At $t = 2$ s, the enrichment factor in the upstream channel reaches $\sim 10^2$ and the concentration in the downstream microchannel is the lowest. The enrichment factor exceeds 10^3, 10^4 and 10^5 at times 14, 200 and 1800 s, respectively, accompanied by the increasing of particle concentration in the downstream. This is because the number of particles overcoming the electric energy barrier at the front of ion depletion zone increases when more particles are accumulated before the barrier. After infinitely long time ($t = \infty$), the system should approach steady state, which could be obtained numerically through stationary analysis (see the dashed curve in Fig. 2(b)). At this state, the number of particles entering the channel through the left boundary is equal to that leaving the channel through the right boundary. The amount of particles inside the channel reaches a constant limiting value, with a million-fold enrichment of particle concentration ($r = 3.2 \times 10^6$).

It has been repeatedly observed in experiments that concentration speed in such micro/nanofluidic system exhibits a complicated, nonlinear characteristics: at the beginning, the concentration speed increases; in the second stage, it is almost a constant and finally, it decreases slowly. To experimentalists, this *concentration speed* is largely approximate, estimated based on the peak concentrations measured through the fluorescence intensity as the metric and the width of the peak. A more rigorous definition of the concentration speed could be defined though the total amount of particles trapped in the upstream microchannel. This corresponds to the time derivative of the integration of particle concentration over the upstream microchannel in Fig. 2(a), or approximately the difference in fluxes at the inlet and outlet boundaries of the microchannel, i.e., $j_{x,3}|_{\text{inlet}} - j_{x,3}|_{\text{outlet}}$ (this includes the amount of particles in the downstream microchannel, which is negligibly small). Figure 3 shows the evolution of integrated particle fluxes over the inlet and outlet boundaries of the microchannel as well as the difference between them. From the solid black curve, we may find that the concentration speed grows by approximately 50% in about 20 s (Stage I), then it is followed by an almost constant concentration speed for a long time (Stage II). At times beyond 10^4 s, the concentration speed decreases gradually to almost zero at time $t = 4 \cdot 10^5$ s (Stage III), after that, the system approaches the steady state (Stage IV). In Stage I, the depletion zone, the electric energy barrier and the vortex-driven electrokinetic flow are developing, bring particles into the microchannel at an increasing speed. After the electric field and the electrokinetic flow become stable, the system enters Stage II with constant feeding rate of the particles. In these two stages, the flux out of the microchannel is negligible compared to that enters the microchannel, with almost all the particles focused. Therefore, an increasing concentration speed in Stage I and a constant concentration speed in Stage II are observed. However, in Stage III, the concentration of particles reaches maximum limiting value and the focused peak expands into the upstream. The flux at the inlet is reduced while the flux at the outlet is increased by strong diffusion of particles into both ends of the channel. As a result, the concentration
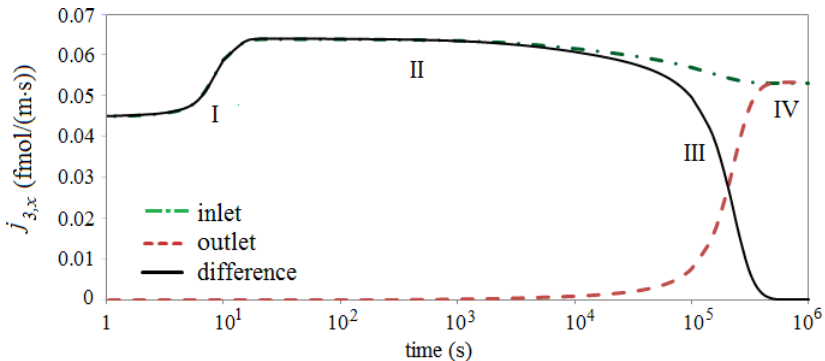

Fig. 3. (Color online) Evolution of concentration speed (solid black curve) expressed as the difference between the fluxes at the inlet (dotted dashed, green) and outlet (dashed, red) boundaries.

speed reduces. Ultimately, the number of particles that enters the microchannel at a unit time becomes equal to that leaves the microchannel at the outlet, and the system reaches a steady state, with zero concentration speed (Stage IV). Although this limiting steady state often needs quite long time to reach, it defines unique behaviors and ultimate functionalities of the system. Thus, we use such steady states for further analyses.

3.2. *Effects of cross-membrane voltage*

As ion depletion and particle enrichment are induced by cross-membrane voltage V_{cm}, it is expected that higher V_{cm} will induce stronger enrichment effect. This tendency is demonstrated in the profiles of particle concentration as shown in Fig. 4. Here, the parameters of the particles are the same as those in Fig. 2 ($Z_3 = -2$, $D_3 = D_2/4$), while V_{cm} is varied in a wide range. It could be found that the enrichment factor increases sharply with V_{cm} when V_{cm} is smaller than $26V_T$, but it becomes saturated (at a value of $r = 3.2 \times 10^6$) beyond that value. Further increasing of V_{cm} does not increase the height of the peak, but broadens it into the upstream. The inset of Fig. 4 shows the relationship between the maximum enrichment factor and V_{cm}. It could be found that there are two distinct phases in the curve. For $V_{cm} < 26V_T$, the enrichment factor grows exponentially with V_{cm}. In this phase, the increasing of V_{cm} strengthens the electric field approximately linearly, which results in an exponentially increasing concentration of particles at the steady state (see Eq. (4)). However, for $V_{cm} > 26V_T$, the concentration of particles becomes so high that they replace almost all the co-ions in the solution. In this scenario, the particle concentration is limited by the concentration of counter ions (decreasing with V_{cm}, cf. Sec. 3.5), and therefore the enrichment factor becomes saturated.
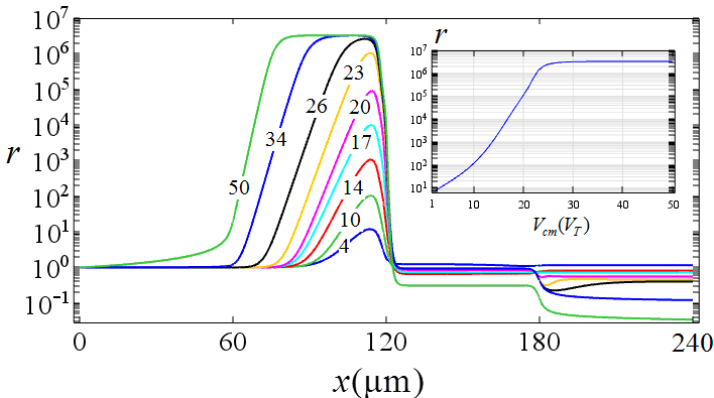

Fig. 4. Steady state profiles of particle concentration along the center line of the microchannel at varied V_{cm} (labels on the curves are V_{cm} in terms of V_T). Inset shows the dependence of the maximum enrichment factor on V_{cm}.

3.3. *Effects of initial particle and buffer ion concentrations*

For a given channel, apart from V_{cm}, two most important factors that may affect the enrichment of particles are the initial particle concentration in the inlet reservoir ($C_{3,0}$) and the concentration of buffer ions (C_0). To investigate these effects, we calculate the limiting concentration of charged particles with varied $C_{3,0}$ and C_0, respectively. Figure 5(a) shows the result at $V_{cm} = 30V_T$, from which we learn that the enrichment factor is generally inversely proportional to $C_{3,0}$, which implies a constant limiting particle concentration inside the microchannel. In fact, the maximum particle concentration (shown in the inset) is very slightly dependent on particle concentration in the inlet reservoir. Specifically, when $C_{3,0}$ increases from 10^{-7} mM to 10^{-2} mM (by an order of 10^5), the limiting focused concentration
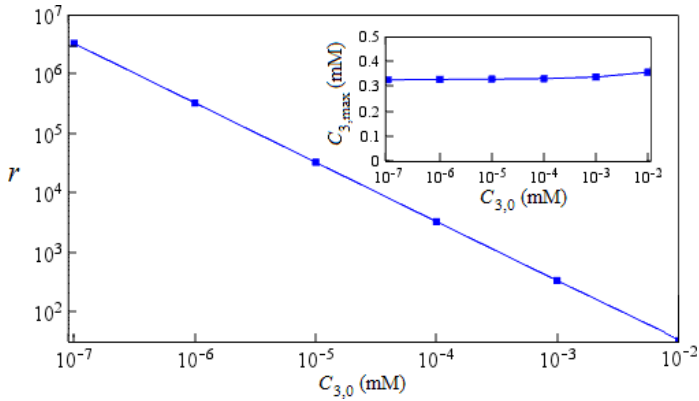
(a)
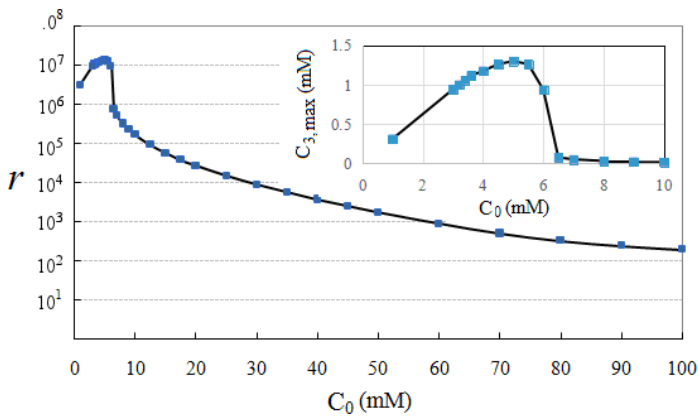
(b)

Fig. 5. Dependence of enrichment factor on (a) initial particle concentration $C_{3,0}$ and (b) the concentration of buffer ions (C_0), with insets showing the maximum particle concentration $C_{3,\max}$ along the center line of microchannel.

grows only from $0.32\,\text{mM}$ to $0.35\,\text{mM}$ (by $\sim 10\%$). Such a variation is practically negligible in most engineering applications.

Figure 5(b) shows the dependence of limiting concentration on the buffer ion concentration. In this example, the initial concentration of particles is fixed at $C_{3,0} = 10^{-7}\,\text{mM}$, while the buffer concentration C_0 changes from $1\,\text{mM}$ to $100\,\text{mM}$ at a constant $V_{\text{cm}} = 30V_T$. It could be seen that for $C_0 \leq 5\,\text{mM}$, the particle enrichment factor grows with C_0, simply because that the upper limit defined by the concentration of K^+ is increased. However, beyond $C_0 = 5\,\text{mM}$, the enrichment factor decreases sharply. At $C_0 = 6.5\,\text{mM}$, the enrichment factor is less than 6% of its value at $C_0 = 0.5\,\text{mM}$ (see the inset). After that, the enrichment factor decreases slowly. The reason behind this complicate behavior lies in the extent of ion depletion. For a given permselective membrane, the amount of counter ions that resides in pore spaces is almost constant (determined by net charges on surfaces of solid phase of membrane and neutrality condition) and there is a limit for the amount of counter ions passing through the membrane at a fixed voltage. If the concentration of buffer ions is low, ion depletion is well developed and strong electric field is built as the energy barrier for charged particles. In this scenario, the increasing buffer concentrations permit more particles to replace buffer co-ions, giving rise to higher enrichment factor. However, if the concentration of buffer ions is so high that ion depletion zone cannot form sufficiently, the electric force that stops the flow of particles becomes weakened and the enrichment effect is compromised consequently. This result provides important insights into some of the experimental observations. Specifically, in the early experiments of preconcentration using relatively pure solutions (e.g., fluorescent proteins and buffer ions), good preconcentration was observed. However, it is generally the case that preconcentration becomes less efficient when carried out over a complex buffer (e.g., serum), often with high-abundance background molecules (e.g., serum albumin or globulins). The result here suggests that one mechanism to explain such behavior, since high abundance background ions and/or molecules, will diminish the formation of the ion depletion and significantly reduce the ultimate possible concentration of particles in the device.

3.4. *Conditions for particles to get enriched*

To study the behavior of particles of different sizes, we consider particles of the same charge ($Z_3 = -2$) but with diameter α times of Cl^- ($D_3 = D_2/\alpha$). Figure 6(a) shows the steady state concentration profiles of particles of different sizes at $V_{\text{cm}} = 14V_T$ (the labels on the curves are values of α). It is obvious that only particles with $\alpha > 2$ are enriched, with $\alpha = 3$ having the best enrichment effect. Particles of $\alpha \leq 2$ are not focused since their viscous drag is not strong enough to bring them into the microchannel with EDF. Figure 6(b) shows the effects of particle charges. Here, the size of particles is fixed ($D_3 = D_2/4$) and the valence n (labeled on the curves) is changed. It is clear that only particles with charges $n < 4$ are focused, with $\alpha = 3$ having the highest enrichment factor.
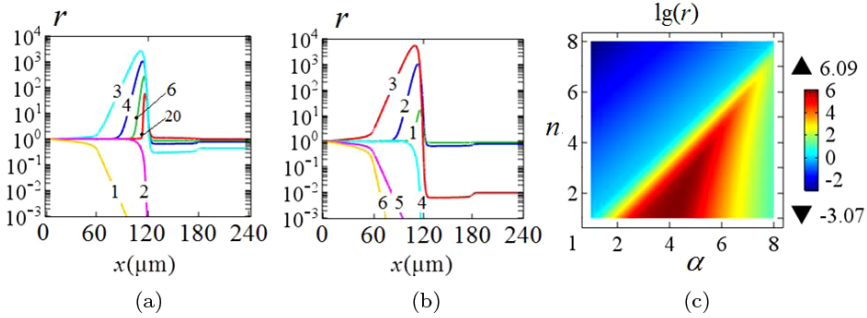
Fig. 6. Steady state concentration profiles of particles of (a) different sizes, (b) different charges and (c) varied sizes and charges at $V_{cm} = 14V_T$.

In principle, the behaviors of particles in this system are governed by interplay between the leftward electrophoretic force ($\propto n$) and the rightward fluidic drag force ($\propto D_3^{-1}$ or α). To permit a particle to enter the channel, magnitude of the viscous drag force must be greater than the electrophoretic force at the channel entrance. Because these two forces are almost equal for Cl$^-$ all over the channel (the flux of Cl$^-$ is close to zero, indicating a nearly zero migration speed and a balanced electrophoretic and drag force, cf. Sec. 3.8), the condition for the particle to enter the channel could be expressed as $n/\alpha < 1$. This condition can be justified by the results in Figs. 6(a) and 6(b), where only particles with $n/\alpha < 1$ get enriched. More detailed study over this condition requires systematic changes of both n and α in a continuous mode. For this purpose, Fig. 6(c) shows the maximum enrichment factor (colored in the order of 10) with varied values of n and α (both from 1.0 to 8.0, at an interval of 0.2). It is clear that there is a partition line with $n/\alpha = 1$, with an enrichment factor of 1.0. Particles with $n/\alpha < 1$ are enriched ($r > 1$), while those with $n/\alpha > 1$ are not enriched ($r < 1$). Bearing in mind that n/α is proportional to the electrophoretic mobility of the particle and $n/\alpha = 1$ is representing buffer co-ion Cl$^-$, the condition for particle enrichment can be expressed as *only particles with the electrophoretic mobility smaller than buffer co-ions can be focused*. It is noteworthy that although $n/\alpha < 1$ guarantees that particles can enter the microchannel with fluid flow, it does not mean that particles with smaller n/α will be *better* focused. In fact, particles with smaller charge or larger size are subject to weaker electric force or higher viscous drag forces, thus are easier to overcome the electric energy barrier before the ion depletion zone and leak into the downstream channel. Therefore, there is a maximum value of enrichment factor for situations of changing either particle size or electric charge, beyond which the enrichment factor of particles of smaller charges or larger particles is reduced (see Fig. 6(c)).

3.5. *Replacement of buffer co-ions by focused particles*

In contrast to particle concentration, which can be measured experimentally, concentrations of buffer ions in such micro/nanofluidic channels have never been
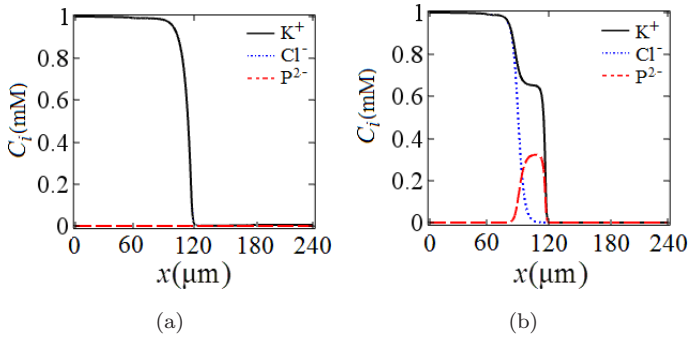
Fig. 7. Concentrations of K^+, Cl^- and P^{2-} at (a) $V_{cm} = 14V_T$ and (b) $V_{cm} = 34V_T$.

measured experimentally or studied numerically (in the presence of concentrating particles). In the end, Figs. 7(a) and 7(b) show the steady state concentration of K^+, Cl^- and P^{2-} at $V_{cm} = 14V_T$ and $V_{cm} = 34V_T$, respectively. In both cases, ion depletion occurs near the membrane location and concentrations of all the charged species are very low in downstream channel. At low V_{cm} (e.g., $14V_T$), concentration of P^{2-} is significantly smaller than that of Cl^- all over the channel (see Fig. 7(a)). In this scenario, the electric field and the EOF are dominated by K^+ and Cl^-. However, if V_{cm} is high (e.g., $34V_T$), K^+ ions are neutralized mainly by P^{2-} in the focused region, leaving an almost-zero concentration for Cl^-, i.e., Cl^- ions are almost completely replaced by P^{2-} (see Fig. 7(b)). This therefore imposes an upper limit on the concentration of P^{2-}: it cannot exceed that required to neutralize K^+. Another important finding from Fig. 7(b) is that the concentration of K^+ in the particle-focused region is non-negligibly lower than that in regions with low concentration of P^{2-}. For example, the concentration of K^+ at $V_{cm} = 34V_T$ is about $0.655\,\mathrm{mM}$ in the replaced region, significantly lower than $1\,\mathrm{mM}$ near the entrance. This variation is determined by the difference in mobilities of P^{2-} and that of Cl^- and the conservation of current. More specifically, near the entrance, concentration of P^{2-} is small, current of negative charges is carried mainly by Cl^- with high mobility. In the meantime near the membrane, this current is carried almost fully by P^{2-} with low mobility. Conservation of the negative charge current requires that the electric field must be higher in the replaced region, so that the negative charges carried by different species have the same phenomenal migration speed. A higher electric field corresponds to a lower concentration of both K^+ and negatively charged species. Therefore, accompanying the replacement of anions by the focused particles, the concentration of buffer K^+ is reduced.

3.6. *Electric field*

The enrichment of particles requires that fluid drag force must be greater than the electrophoretic force at the entrance of microchannel, while in the mean time, the later must be greater than the former somewhere inside. This requirement has to be
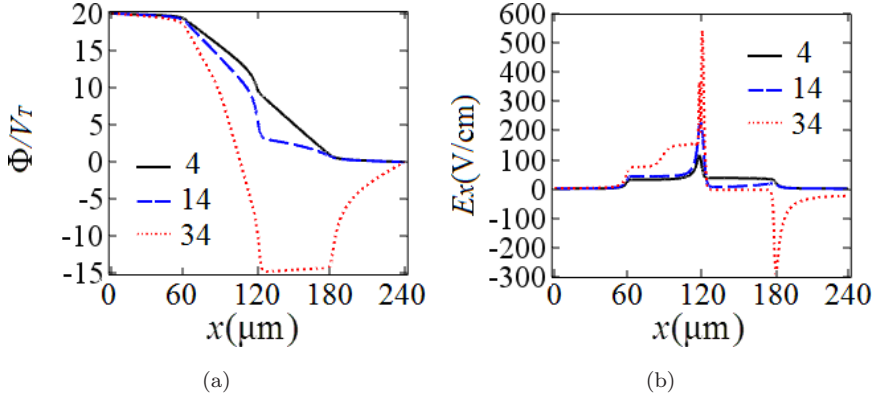
Fig. 8. (a) Electric potential and (b) electric field along the center line at varied V_{cm}. It is noteworthy that the electric field in the particle focused region is much higher than that in the buffer ion-dominated region at high cross-membrane voltage $V_{cm} = 34V_T$. This is a consequence of almost full replacement of buffer co-ions by the focused particles and simultaneous decreasing of counter ion concentration (cf. Sec. 3.5).

fulfilled by the variation of electric field [Kim *et al.*, 2009], because the average fluid flow speed is constant all over the microchannel, determined by the conservation of fluid.

Figure 8 gives profiles of electric potential Φ along the center line of the channel and the corresponding electric field component E_x at varied V_{cm}. At low V_{cm}, values of Φ and E_x are generally dominated by the channel geometry and values of V_L and V_R. Increasing of V_{cm} lowers Φ near the membrane and in the downstream microchannel, elevates E_x in the upstream channel and decreases it in downstream. For example, at $V_{cm} = 34V_T$, the maximum value of E_x in the front of the depletion zone is ~542 V/cm, nearly 25 times of the channel average value defined by V_L and V_R (21.5 V/cm). In addition, at $V_{cm} > 18V_T$, the direction of the electric field in the downstream microchannel is reversed ($E_x < 0$, although its magnitude is very small. This inversed magnitude is to compensate the difference between the total fluxes of ions and particles and their respective convective fluxes in the downstream microchannel. Further increase of V_{cm} induces significantly stronger electric fields within the microchannel in the upstream, and outside the microchannel in the down stream. Meanwhile, the electric fields in the downstream microchannel remain significantly weaker (see the flat bottom of the electric potential profile at $V_{cm} = 34V_T$ in Fig. 8(a)), because the transport of charged species is dominated by the convective flux driven by fast fluid flow. Reverse of electric field direction in downstream microchannel has been reported experimentally [Kim *et al.*, 2009].

3.7. *Pumping effect*

Accompanying ion depletion and formation of extended space charge near the membrane surface, the fluid nearby is accelerated and rotating vortices are generated
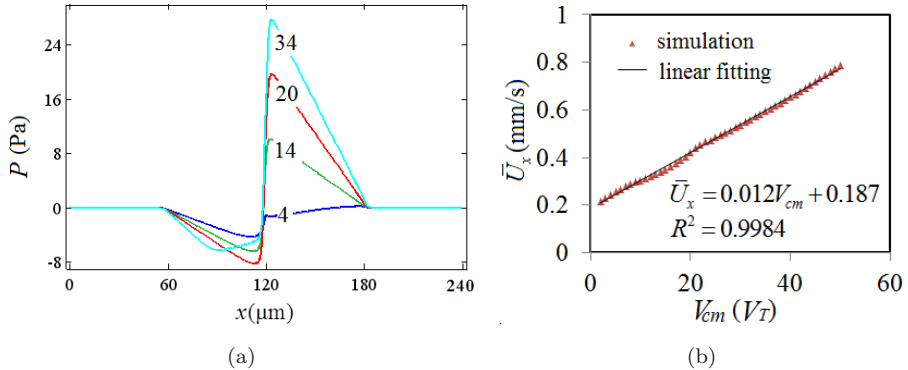
Fig. 9.   (a) Pressure distribution along the center of the channel and (b) dependence of the average flow speed on cross-membrane voltage.

under the amplified electric field. These vortices decrease the pressure in the upstream channel and increase the pressure in downstream, i.e., a fluid pumping effect is generated (see Fig. 9(a)). This effect has been studied qualitatively through experimental observations [Kim *et al.*, 2009]. More insights into this effect could be obtained from the largely linear relationship between the average fluid flow speeds and V_{cm} as shown in Fig. 9(b). From the fitted expression, we may identify the contribution from the traditional EOF (U_x at $V_{cm} = 0$) and that from the ICP effect (the difference between the actual $\bar{U}_x$ and that caused by EOF). For example, at $V_{cm} = 50V_T$ the average fluid flow speed is $0.79\,\mathrm{mm/s}$. The contribution from ICP effect is about 3.4 times of that from EOF ($0.18\,\mathrm{mm/s}$). This pumping effect demonstrates an additional advantage of this system: it speeds up the particle preconcentration processes by several times.

3.8. *Fluxes of charged species*

Figure 10 depicts the steady state fluxes of K^+ (red arrows in Fig. 10(a)) and negatively charged species (Cl^- and P^{2-}, blue arrows in Fig. 10(b)), along with the streamline of the fluid flow. For clarification purposes, fluxes for negatively charged species in Fig. 10(b) are magnified eight times (as compared with those of K^+ in Fig. 10(a)), because their magnitudes are small. In contrast to simple flux profile of K^+ that enters the microchannel and flows out through the membrane, flux field of negative species is complicated. There is a counterclockwise vortex influx of negatively charged species near the membrane in the upstream channel (driven largely by fluidic vortex, shown in black color). While at the far end of upstream channel, there is a clockwise flux vortex as a result of balance between the non-uniform rightward fluidic flow and leftward electrophoretic motion. In the region where these two vortices meet, the fluxes of negative particles are almost zero. If we integrate the fluxes of each species over cross-section (cs) of the channel $j_{x,i} = \int_{cs} J_{x,i} dy$, $i = 1, 2, 3$, we get a constant large flux for K^+ ($j_{x,1}$), and a constant near-zero flux
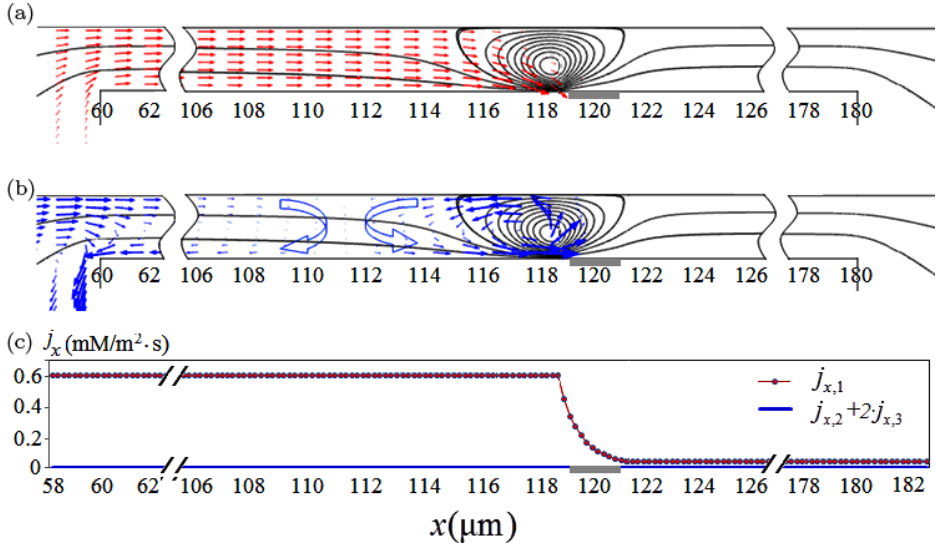
Fig. 10. (a) Flux field of K$^+$ at $V_{cm} = 10V_T$; (b) distribution of total negative charge fluxes (Cl$^-$ and P^{2-}) and (c) profiles of one-dimensional projected fluxes. Locations of membrane are highlighted by thick gray lines.

for negative charges ($j_{x,2} + 2j_{x,3}$) in the upstream microchannel (see Fig. 10(c)). While, in the downstream, fluxes of all the charged species are almost zero. In other words, in one-dimensional description, counter ions enter the microchannel and leave the channel through the membrane, while negatively charged species are *almost* stationary at the steady state. These descriptions are also valid for time-dependent data, although replacement of Cl$^-$ by P^{2-} takes place, until the steady state is reached.

3.9. *Mechanism picture of electric field-driven preconcentration*

The integration of results described above permits us to draw a full mechanism picture for transport of cations, anions, particles and the solvent fluid collectively in a micro/nanofluidic channel with ICP. Application of V_{cm} induces ion depletion that (1) desalinates the solution in the downstream; (2) stops the motion of co-ions and particles and (3) speeds up the fluid flow as a pump. If the electrophoretic mobilities of the particles are smaller than the buffer co-ions, particles enter the microchannel with fluid and accumulate at the front of the depletion zone and replace co-ions. During this process, (1) fluid flows at a constant speed; (2) co-ions are almost stationary and get slowly replaced by the focused particles and (3) counter ions enter the microchannel and escape through the membrane at a high speed. In the mean time, replacing anions with charged particles decreases the concentration of cations, which further set limits for the concentration of charged particles and anions. As a result, a plateau of particle concentration is formed and

expands to the upstream channel at high V_{cm}. These particle accumulation and ion replacement processes proceed until a steady state is reached.

This mechanism picture may provide new, fundamental guidelines for researchers to explain their experimental observations. For example, one may think that behaviors of negatively charged particles and that of buffer anions should be similar in the sense of transport dynamics and/or enrichment. Simulation results here clarify these misunderstandings by highlighting the diverse dynamics of various charged species (see Fig. 11) and totally different distributions of co-ions and the charged particles (see Fig. 7). These results tell us that one simply cannot infer concentration of anions based on that of the co-charged particles. The second common misunderstanding is that the buffer ions will get enriched, as speculated based on the observation of the focused particle concentration. The actual situation is that focusing of charged particles will reduce the concentrations of both co-ions and counter ions (see Fig. 7). Another common practice, to observe fluid vortices using charged fluorescent particles, is also not safe, because the shape of the vortical flow field of fluid is different from that of particle flux (see Fig. 10(b)).

In theoretical aspects, the analyses of such systems have been often conducted through decoupling electrodynamics flow of electrolytes and convective diffusion of charged particles. This treatment may not work in most actual preconcentration situations because the basic assumption for such treatment, i.e., particle enrichment does not affect the fluid flow and distribution of buffer ions, becomes invalid when the charge carried by the focused particles is not negligible compared with that carried by buffer co-ions. For example, if we use decoupled model (to calculate fields of the fluid velocity, pressure and electric potential first without the presence of particle, and then use these fields to calculate the convective diffusion of charged particles in these constant fields) to calculate the enrichment factor at
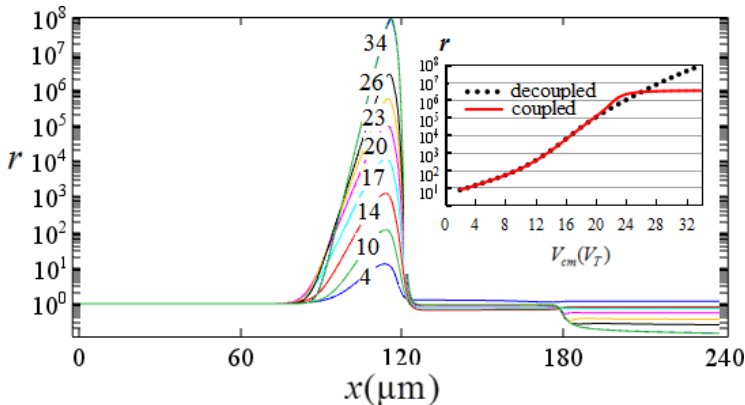

Fig. 11. Steady state profiles of particle concentration along the center line of the microchannel at varied V_{cm} (labels on the curves are V_{cm} in terms of V_T) using a decoupled model. The inset shows the maximum enrichment factors predicted by coupled and decoupled models.

varied cross-membrane voltage (cases in Fig. 4), we will get an ever growing enrichment factor without upstream band expansion (see Fig. 11). As shown in the inset, the two systems produce almost identical results at low $V_{cm} \leq 20V_T$. However, the results of the decoupled model at $V_{cm} > 20V_T$ are completely unreasonable. For example, at $V_{cm} = 34V_T$, the enrichment factor reaches $\sim 10^8$, corresponding to a particle concentration ~ 10 times higher than buffer ions. Because the enrichment factor at $V_{cm} = 20V_T$ is $\sim 10^5$, corresponding to a particle concentration of $\sim 0.01\,\mathrm{mM}$ and charges carried by particles ~ 0.02 times of that of Cl^-. This offers us a simple *post priori* criterion for validity of the decoupled model: the charge carried by the focused particle should be less than $\sim 2\%$ of that carried by buffer co-ions. If a decoupled model yields a particle concentration with charges less than this value, the results are safe, otherwise they are not reliable and need revision. From these discussions, we know that charged particles in such systems are playing active roles in such systems through contribution to the charge density of the fluid and mediating the electric field. This may further affect the flow of fluids and transport of buffer ions. These fundamental understandings will significantly help future researches in the analysis of experimental results or design of similar microfluidic systems.

Finally, it should be emphasized that the particles considered in this paper are point-size Brownian particles. It has a fixed charge and a Stokes radius, which is used only in calculating the friction forces from the fluid. This treatment is valid for most inorganic ions and small biomolecules like peptides. Large particles with the detailed structures and/or induced charge phenomena are not considered here.

4. Conclusions

This paper describes the full mechanism picture of particle preconcentration micro/nanofluidic system through accurate multi-physics simulation. Dynamics of fluids and charged species are analyzed through time-dependent and steady state analyses. Effects of cross-membrane voltages, charge, size and initial concentration of the particle, buffer ion concentrations are elaborated. Conditions for particles that are able to be concentrated are identified. Several key processes that are difficult to quantify in experiments, such as the replacement of buffer co-ions by focused particles, fluxes of ions and particles, pumping effects, and distribution of electric fields are clearly described. The validity of decoupled simulation model is discussed. Such fundamental knowledge provides a new way of analyzing experimental results, especially when phenomena that are not directly observable (such as dynamics of buffer ions, and fluid–particle interactions) are involved. The results and findings of this simulation have great potential in guiding the device design and protocol development of all similar micro/nanofluidic preconcentration systems, including single channel preconcentration [Ko *et al.*, 2012; Kim *et al.*, 2013; Choi *et al.*, 2015; Lee *et al.*, 2016], integration of particle preconcentration with subsequent separation, etc. [Inglis *et al.*, 2011; Chen *et al.*, 2016].

Acknowledgments

References

Auroux, P. A., Iossifidis, D., Reyez, D. R. and Manz, A. [2002] "Micro total analysis systems. 2. Analytical standard operations and applications," *Analytical Chemistry* **74**(12), 2637–2652.

Bocquet, L. and Charlaix, E. [2010] "Nanofluidics, from bulk to interfaces," *Chemical Society Reviews* **39**(3), 1073–1095.

Çetin, B., Özer, M. B. and Solmaz, M. E. [2014] "Microfluidic bio-particle manipulation for biotechnology," *Biochemical Engineering Journal* **92**, 63–82.

Chen, Y. Y., Chiu, P. H., Weng, C. H. and Yang, R. J. [2016] "Preconcentration of diluted mixed-species samples following separation and collection in a micro-nanofluidic device," *Biomicrofluidics* **10**(1), 014119.

Choi, D., Choi, A. and Dong, S. K. [2015] "A capillary-based preconcentration device by using ion concentration polarization through cation permselective membrane coating," *International Journal of Precision Engineering and Manufacturing* **16**(7), 1467–1471.

Deng, D. S., Aouad, W., Braff, W. A., Schlumpberger, S., Suss, M. E. and Bazant, M. Z. [2015] "Water purification by shock electrodialysis: Deionization, filtration, separation and disinfection," *Desalination* **357**, 77–83.

Drozdov, A. D. and Christiansen, J. D. [2016] "The effects of ph and ionic strength of swelling of cationic gels," *International Journal of Applied Mechanics* **08**(05), 1650059.

Druzgalski, C. L., Andersen, M. B. and Mani, A. [2013] "Direct numerical simulation of electroconvective instability and hydrodynamic chaos near an ion-selective surface," *Physics of Fluids* **25**(11), 8316–8322.

Dydek, E. V., Zaltzman, B., Rubinstein, I., Deng, D. S., Mani, A. and Bazant, M. Z. [2011] "Overlimiting current in a microchannel," *Physical Review Letters* **107**(11), 118301.

Hlushkou, D., Knust, K. N., Crooks, R. M. and Tallarek, U. [2016] "Numerical simulation of electrochemical desalination," *Journal of Physics Condensed Matter* **28**(19), 194001.

Inglis, D. W., Goldys, E. M. and Calander, N. P. [2011] "Simultaneous concentration and separation of proteins in a nanochannel," *Angewandte Chemie* **50**(33), 7546–7550.

Karatay, E., Druzgalski, C. L. and Mani, A. [2015] "Simulation of chaotic electrokinetic transport: Performance of commercial software versus custom-built direct numerical simulation codes," *Journal of Colloid and Interface Science* **446**, 67–76.

Kim, M., Jia, M. and Kim, T. [2013] "Ion concentration polarization in a single and open microchannel induced by a surface-patterned perm-selective film," *Analyst* **138**(5), 1370.

Kim, S. J., Ko, S. H., Kang, K. H. and Han, J. [2010a] "Direct seawater desalination by ion concentration polarization," *Nature Nanotechnology* **5**(4), 297–301.

Kim, S. J., Song, Y. A. and Han, J. [2010b] "Nanofluidic concentration devices for biomolecules utilizing ion concentration polarization: Theory, fabrication and applications," *Chemical Society Reviews* **39**(3), 912.

Kim, S. J., Li, L. D. and Han, J. [2009] "Amplified electrokinetic response concentration polarization near nanofluidic channel," *Langmuir* **25**(13), 7759–7765.

Ko, S. H., Song, Y. A., Kim, S. J., Kim, M., Han, J. and Kang, K. H. [2012] "Nanofluidic preconcentration device in a straight microchannel using ion concentration polarization," *Lab on A Chip* **12**(21), 4472.

Lee, S. J., Rhee, H., Jeon, T. J. and Kim, D. [2016] "Preconcentration of lipid vesicles using concentration polarization in a microfluidic chip," *Sensors and Actuators B Chemical* **229**, 276–280.

Li, B., Chen, H. and Li, D. [2016] "Effect of solvent diffusion on reactive chromotropic polyelectrolyte gel," *International Journal of Applied Mechanics* **08**(07), 1640008.

Li, M. and Anand, R. K. [2016] "Recent advancements in ion concentration polarization," *Analyst* **141**(12), 3496–3510.

Lin, C. C., Hsu, J. L. and Lee, G. B. [2011] "Sample preconcentration in microfluidic devices," *Microfluidics and Nanofluidics* **10**(3), 481–511.

Liu, W., Gong, L. Y., Zhu, Y. D. and Li, Z. R. [2018] "Augmented electroosmotic flow and simultaneous desalination in microchannels embedded with permselective membranes (in Chinese)," Scientia Sinica Technologica, 46, doi: 10.1360N092017-00034.

Mani, A., Zangle, T. A. and Santiago, J. G. [2009] "On the propagation of concentration polarization from microchannel-nanochannel interfaces. Part I: Analytical model and characteristic analysis," *Langmuir* **25**(6), 3898.

Napoli, M., Eijkel, J. C. and Pennathur, S. [2010] "Nanofluidic technology for biomolecule applications: A critical review," *Lab on A Chip* **10**(8), 957.

Nikonenko, V. V., Kovalenko, A. V., Urtenov, M. K., Pismenskaya, N. D., Han, J. and Sistat, P. *et al.* [2014] "Desalination at overlimiting currents: State-of-the-art and perspectives," *Desalination* **342**(5), 85–106.

Pham, V. S., Li, Z., Lim, K. M., White, J. K. and Han, J. [2012] "Direct numerical simulation of electroconvective instability and hysteretic current–voltage response of a permselective membrane," *Physical Review E, Statistical Nonlinear and Soft Matter Physics* **86**(4), 046310.

Rubinstein, I. I. and Zaltzman, B. [2000] "Electro-osmotically induced convection at a permselective membrane," *Physical Review E, Statistical Physics Plasmas Fluids and Related Interdisciplinary Topics* **62**(2), 2238.

Rubinstein, I. and Zaltzman, B. [2015] "Equilibrium electroconvective instability," *Physical Review Letters* **114**(11), 114502.

Shen, M., Yang, H., Sivagnanam, V. and Gijs, M. A. [2010] "Microfluidic protein preconcentrator using a microchannel-integrated nafion strip: Experiment and modeling," *Analytical Chemistry* **82**(24), 9989.

Sparreboom, W., Berg, A. V. D. and Eijkel, J. C. T. [2010] "Transport in nanofluidic systems: A review of theory and applications," *New Journal of Physics* **12**(3), 338–346.

Wang, Y., Pant, K., Chen, Z., Wang, G., Diffey, W. F., Ashley, P. and Sundaram, S. [2009] "Numerical analysis of electrokinetic transport in micro-nanofluidic interconnect preconcentrator in hydrodynamic flow," *Microfluidics and Nanofluidics* **7**(5), 683–696.

Wang, Y. C., Stevens, A. L. and Han, J. [2005] "Million-fold preconcentration of proteins and peptides by nanofluidic filter," *Analytical Chemistry* **77**(14), 4293–4299.

Yossifon, G., Chang, Y. C. and Chang, H. C. [2009] "Rectification, gating voltage and interchannel communication of nanoslot arrays due to asymmetric entrance space charge polarization," *Physical Review Letters* **103**(15), 154502.

Zangle, T. A., Mani, A. and Santiago, J. G. [2009] "On the propagation of concentration polarization from microchannel-nanochannel interfaces. Part II: Numerical and experimental study," *Langmuir* **25**(6), 3909–3916.

Zangle, T. A., Mani, A. and Santiago, J. G. [2010a] "Theory and experiments of concentration polarization and ion focusing at microchannel and nanochannel interfaces," *Chemical Society Reviews* **39**(3), 1014–1035.

Zangle, T. A., Mani, A. and Santiago, J. G. [2010b] "Effects of constant voltage on time evolution of propagating concentration polarization," *Analytical Chemistry* **82**(8), 3114.